Konya Mühendislik Bilimleri Dergisi, c. 13, s. 2, 546-567, 2025
Konya Journal of Engineering Sciences, v. 13, n. 2, 546-567, 2025
ISSN: 2667-8055 (Electronic)
DOI: 10.36306/konjes.1585324

CRAMER-RAO LOWER BOUND ANALYSIS FOR MAGNETIC LOCALIZATION OF A ROBOTIC CAPSULE ENDOSCOPE

[1, *]Muzaffer KANAAN, [2]Muhammed CİL, [3]Memduh SUVEREN

[1, 3] Erciyes University, Mechatronics Engineering Department, Kayseri, TÜRKİYE
[2] Kafkas University, Mechanical Engineering Department, Kars, TÜRKİYE
[1]mkanaan@erciyes.edu.tr , [2]muhammed.cil@kafkas.edu.tr, [3]msuveren@erciyes.edu.tr

Highlights

- A performance analysis is presented for magnetic wireless capsule localization.
- The analysis is based on the Cramer-Rao Lower Bound.
- Performance dependency on a number of system parameters is explored.
- The capsule can be localized inside the body with sub-millimeter accuracy.

Graphical Abstract

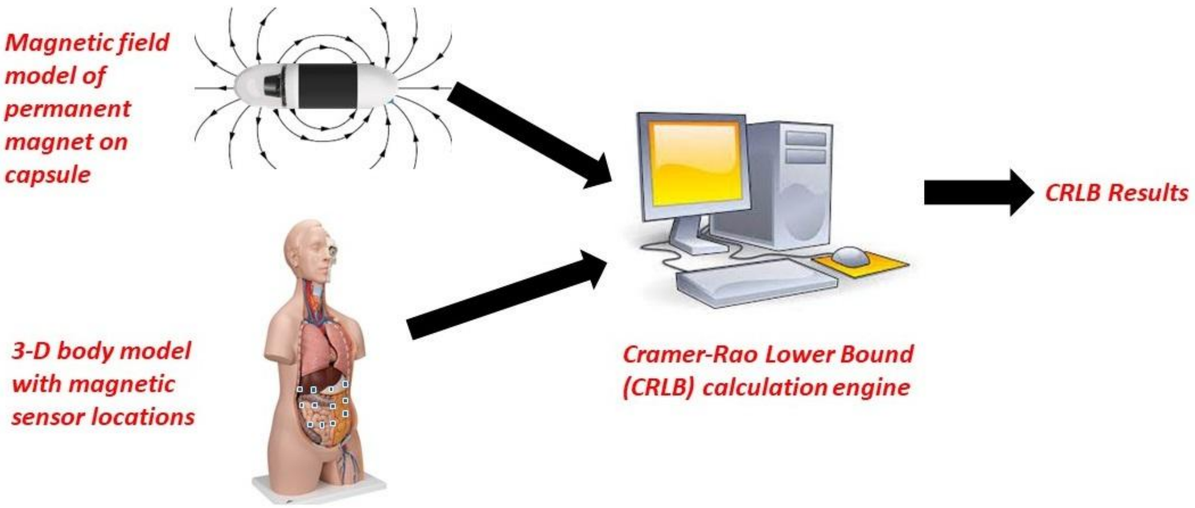

***Corresponding Author:** Muzaffer KANAAN, mkanaan@erciyes.edu.tr

Konya Mühendislik Bilimleri Dergisi, c. 13, s. 2, 546-567, 2025
Konya Journal of Engineering Sciences, v. 13, n. 2, 546-567, 2025
ISSN: 2667-8055 (Electronic)
DOI: 10.36306/konjes.1585324

CRAMER-RAO LOWER BOUND ANALYSIS FOR MAGNETIC LOCALIZATION OF A ROBOTIC CAPSULE ENDOSCOPE

[1,*]Muzaffer KANAAN , [2]Muhammed CİL, [3]Memduh SUVEREN

[1,3] *Erciyes University, Mechatronics Engineering Department, Kayseri, TÜRKİYE*
[2] *Kafkas University, Mechanical Engineering Department, Kars, TÜRKİYE*
[1]mkanaan@erciyes.edu.tr , [2]muhammed.cil@kafkas.edu.tr, [3]msuveren@erciyes.edu.tr

ABSTRACT: In robotic capsule endoscopy, highly accurate localization of the capsule device inside the human body is a critical problem for disease diagnosis and treatment. Quantitative analysis of lower bounds, such as the Cramer-Rao Lower Bound, is practically important for localization systems, as they inform system designers of the best achievable performance under a given set of conditions. This paper presents a comprehensive, systematic analysis of the Cramer-Rao Lower Bound for the scenario of magnetic localization of a robotic wireless capsule endoscope inside the human body. The specific contributions of the study are threefold. First, we undertake a systematic analysis of the bound in the presence of a realistic 3D body model. Second, we present a detailed analysis of the effects of capsule motion as well as other system parameters (such as magnet type and magnet dimensions) inside the body on the bound values. Finally, we interpret the findings to come up with recommendations on system parameters to guarantee optimal performance.

Keywords: *Cramer-Rao Lower Bound, Magnetic Localization, Robotic Capsule Endoscopy*

1. INTRODUCTION

Wireless capsule endoscopy (WCE) technology is rapidly becoming a very popular medical imaging technique, especially for the diseases of the gastrointestinal (GI) tract[1-3]. This is because WCE technology is minimally invasive (the patient only has to swallow a capsule) and painless for the patient in contrast to conventional endoscopy, where the patient typically has to be sedated. As a result, clinical use of WCE has been extended to imaging other parts of the GI tract, such as the stomach, esophagus, duodenum and the colonic mucosa[4, 5]. Current generation of WCE systems used in clinical settings are commonly classified as *passive* devices, in the sense that external control of the capsule inside the GI tract is not possible; the capsule moves through the GI tract via standard muscle contractions and is naturally excreted out of the body.

In recent years, WCE technology started to evolve towards *active*, or *robotic* capsule endoscopy (RCE) [6-8]. In contrast to WCE systems, an RCE capsule now becomes a small-size robot, whose motion can be externally controlled. This expands the functionality of the endoscopy capsule, in that the medical specialist can now maneuver the expanse of the GI tract at will, bypassing regions that are not of interest, and focusing more on areas deemed worthy of detailed examination (such as a suspicious tumor, or a lesion, for example). Furthermore, an RCE capsule fitted with adequate sensors and actuators can even carry out other tasks (such as collection of biopsy samples from a tumor, or even ablation of the tumor in a minimally invasive manner). The specific focus of this paper is on RCE systems.

Ever since WCE systems first appeared in clinical settings, the problem of localizing the capsule inside the GI tract has been of interest, since WCE images without corresponding location data are clinically meaningless for diagnosis and treatment purposes. This *localization problem* has previously been studied in considerable detail [9-11]. Much of this research has focused on passive WCE systems. Accurate solution to the localization problem becomes even more critical in an RCE setting, where the user (i.e. the medical

***Corresponding Author:** Muzaffer KANAAN, mkanaan@erciyes.edu.tr

specialist) has to know precisely where the capsule is, on a real-time basis, in order to guide the capsule inside the GI tract for an efficient and thorough medical examination.

There are several methods proposed in the literature for localizing a capsule endoscope device inside the GI tract. These methods include RF localization (i.e. using the RF signal emitted by the capsule to relay images for localization purposes) [12], MR and ultrasound [13], X-ray and Gamma-ray imaging [14], hybrid methods (such as those that leverage RF localization with image processing)[15, 16], and magnetic localization [17]. RF localization, while a very attractive option in principle, has serious accuracy issues when used on its own. This is due to the severe way the RF signal is distorted by the human body tissues (as body tissues have different electrical characteristics, which are also frequency-dependent) [3]. The use of MR and ultrasound techniques may require additional components inside the capsule itself, which is already constrained in terms of size[18, 19]. The use of X-rays and Gamma-rays, while technically an option, are not advisable, as they expose the patient to potentially dangerous amounts of ionizing radiation[20]. Hybrid methods, such as those that use RF localization in conjunction with the processing of received capsule images, are another option; however, this may result in increased computational load, which goes against the real-time localization requirements for RCE systems. This leaves magnetic localization as the most promising alternative option for accurate, real-time localization [21]. As such, this paper focuses on magnetic localization of an RCE capsule inside the GI tract.

In a magnetic localization system, the location-dependent magnetic field from a magnet is sensed by magnetic field sensors and used to come up with a location estimate. Thus, a small permanent magnet located on the capsule can be used to localize the capsule inside the GI tract. Magnetic localization is the most accurate for WCE and future RCE systems, due to the fact that human body tissues have the same magnetic characteristics as free space; therefore, the magnetic field emitted by the permanent magnet is not affected by the body tissues, thus reducing the localization problem to that of localizing a magnetic field source in free space.

For any localization system, the main performance indicator is the localization accuracy, defined as the error between the actual location of the capsule and the location determined by a localization algorithm. This brings up another important question: for a given system scenario and system parameter set, what is the best achievable localization accuracy? Answering this question is of paramount importance for design and performance optimization of localization algorithms. Statistical lower bounds, such as the Cramer-Rao Lower Bound (CRLB), can be used to address this question. In this paper, we present a systematic analysis of the CRLB for magnetic localization of an endoscopy capsule in an RCE scenario.

Although an initial analysis of the CRLB for magnetic localization of an endoscopy capsule was presented in [22], we believe that the analysis needed to be considerably extended, in order to be valid for our RCE scenario. This forms the main motivation of the current paper. The results reported in [22] focused, for the most part, on a planar arrangement of sensors. In a practical scenario, where the sensors are typically on the body surface, this is not realistic. In addition, for magnetic localization, there are other system-related parameters which affect performance, such as magnet size, and magnetic materials. The dependence of the CRLB on such system-related parameters is missing in [22], and could be extremely useful to system designers.

The specific contributions of this paper can be summarized as follows. First, we undertake the CRLB analysis using a realistic 3-D human body model. Second, we present a detailed analysis of the effects of capsule motion inside this body model on the CRLB. Third, we explore the dependence of the CRLB on system-related parameters, such as magnet size and magnetic materials. Finally, we interpret the findings to come up with fundamental recommendations on system parameters to guarantee optimal performance.

The rest of this paper is organized into three sections. Section 2 ("Material and Methods") gives a general overview of magnetic localization techniques, the Cramer-Rao Lower Bound and presents the theoretical framework for the performance evaluation in subsequent sections. Section 3, titled "Results and Discussion", presents the results of the CRLB analysis, based on different practical system scenarios of interest. The paper ends with concluding remarks in Section 4.

2. MATERIAL AND METHODS

2.1 Magnetic Localization Techniques

The magnetic localization technique is based on a small magnet placed on the capsule, which does not require a power supply and connection cable. The magnet attached to the capsule creates a static magnetic field around the human body as it moves with the capsule. This magnetic field can be measured by N magnetic sensors placed on the surface of the patient's body, where N is the number of sensors. Since the magnetic field measured by the sensors depends on the 3-dimensional coordinates and orientation angles in the magnetic field distribution, the capsule position and orientation can be determined by solving an inverse problem.

In order to determine the mathematical expression of the magnetic field distribution in free space, various models can be used[23]. One such model is the magnetic dipole model, preferred in many studies due to its simplicity[24]. The dipole model is based on the equations of magnetic field strength and magnetic flux density emitted by the magnet. The dipole model created for the capsule is based on a cylindrical permanent magnet, as shown in Fig. 1. The capsule diameter is expressed as R1, while the diameter of the magnet surrounding the capsule is expressed as R2

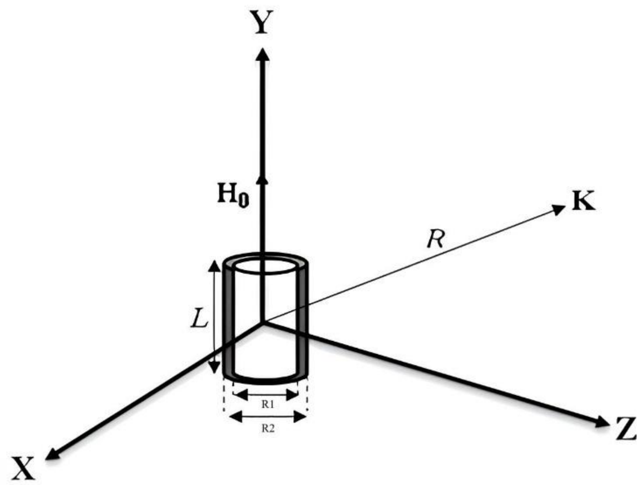

Figure 1. Magnetic field produced by a cylindrical magnet

In this study, a cylindrical magnet geometry, hollow in the inside, is assumed (see Fig. 2), such that the magnet is wrapped over the actual capsule. This ensures that the overall physical size of the capsule does not increase noticeably, thereby allowing the capsule to move more easily through the body and preserving the usability of the device.

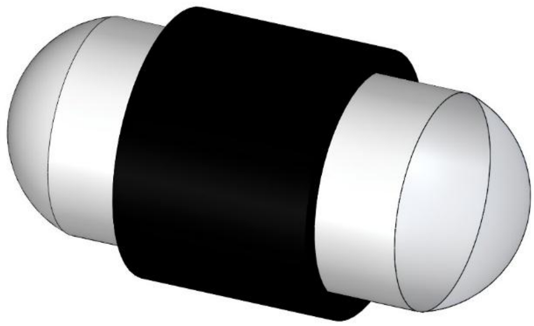

Figure 2. Structure of the capsule including the cylindrical permanent magnet

The dipole model to characterize the magnetic flux density is given by

$$\mathbf{B} = B_T\left(\frac{3(\mathbf{H_0}\cdot\mathbf{K})\mathbf{K}}{R^5} - \frac{\mathbf{H_0}}{R^3}\right) \tag{1}$$

where r_1 and r_2 represent the inner and outer radius of the magnet, respectively. The parameter L represents the length of the magnet and $\mathbf{K} = (x_i, y_i, z_i)^T$ is a spatial point in the Cartesian coordinate system of the magnet, where the magnetic field strength is observed. In addition, R shows the distance between the magnet and $\mathbf{K}$, while $\mathbf{H}_0$ shows the orientation vector of the magnet. The parameter B_T is expressed as $B_T = \frac{\mu_r \mu_0 M_T}{4\pi}$ and $M_T = \pi(r_2^2 - r_1^2)LM_0$, where M_0 is the uniform magnetization (A/m). Relative permeability is represented by μ_r, and $\mu_0 = 4\pi\times10^{-7}$ (H/m) is the magnetic permeability of free space.

The magnetic flux density measured by the i-th sensor is given by

$$\boldsymbol{B}_i = B_{x,i}\hat{\boldsymbol{x}} + B_{y,i}\hat{\boldsymbol{y}} + B_{z,i}\hat{\boldsymbol{z}} \;\; (i = 1, \ldots, N) \tag{2}$$

Axial magnetic flux density expressions can be written as

$$B_{x,i} = B_T\left\{\frac{3\left[m(x_i-a)+n(y_i-b)+p(z_i-c)\right](x_i-a)}{R_i^5} - \frac{m}{R_i^3}\right\} \tag{3}$$

$$B_{y,i} = B_T\left\{\frac{3\left[m(x_i-a)+n(y_i-b)+p(z_i-c)\right](y_i-b)}{R_i^5} - \frac{n}{R_i^3}\right\} \tag{4}$$

$$B_{z,i} = B_T\left\{\frac{3\left[m(x_i-a)+n(y_i-b)+p(z_i-c)\right](z_i-c)}{R_i^5} - \frac{p}{R_i^3}\right\} \tag{5}$$

where (x_i, y_i, z_i) are the known coordinates of the i-th sensor and $R_i = \sqrt{(x_i-a)^2+(y_i-b)^2+(z_i-c)^2}$. Equations (3)-(5) form the basis for the calculation of the CRLB, as discussed in the next section.

2.2. Analysis Of The Magnetic Localization Technique Using The CRLB

The Cramer-Rao Lower Bound (CRLB) represents a lower bound on the error covariance of an unbiased estimator, of some unknown parameter vector $\varepsilon = [\varepsilon_1, \varepsilon_2, \cdots \varepsilon_k]^T$ based on a set of observations[25-30] . The bound is based on the probability density function, $p(\mathrm{x}/\varepsilon)$, of the observation vector $\mathbf{x}$, conditioned on the *deterministic*, unknown parameter vector, $\boldsymbol{\varepsilon}$. Let the vector $\tilde{\boldsymbol{\varepsilon}}$ represent the vector of estimated parameters. The CRLB can then be expressed as

$$cov_\varepsilon(\tilde{\boldsymbol{\varepsilon}}) \geq \boldsymbol{J}_{\boldsymbol{\varepsilon}}^{-1} \tag{6}$$

where $cov_\varepsilon(\tilde{\boldsymbol{\varepsilon}}) = E\{(\tilde{\boldsymbol{\varepsilon}} - \boldsymbol{\varepsilon})(\tilde{\boldsymbol{\varepsilon}} - \boldsymbol{\varepsilon})^T\}$ is the $K\times K$ covariance matrix of the estimation error and $\mathbf{J}_\varepsilon$ is the $K\times K$ Fisher information matrix. For the purposes of the capsule localization problem, $\mathbf{x} = \hat{\mathbf{B}}(\varepsilon)$, where $\hat{\mathbf{B}}$ is the vector of observed magnetic flux density values, that is a function of the unknown location and orientation parameters, $\boldsymbol{\varepsilon} = [a,b,c,m,n,p]^T$, and thus K = 6. The (j,k) element of the Fisher information matrix is defined as

$$\left[\mathbf{J}_{\varepsilon}\right]_{jk} = E_{\varepsilon}\left\{\frac{\partial}{\partial \varepsilon_j}\log p\left(\hat{\mathbf{B}}\middle|\varepsilon\right)\cdot\frac{\partial}{\partial \varepsilon_k}\log p\left(\hat{\mathbf{B}}\middle|\varepsilon\right)\right\} \tag{7}$$

The starting point for the calculation of the CRLB is an observation model, which expresses the noisy measurements of the components of the magnetic flux density from the capsule. This model is given by

$$\begin{aligned} \hat{B}_{x,i} &= B_{x,i}\left(a,b,c,m,n,p\right)+n_{x,i} \\ \hat{B}_{y,i} &= B_{y,i}\left(a,b,c,m,n,p\right)+n_{y,i} \\ \hat{B}_{z,i} &= B_{z,i}\left(a,b,c,m,n,p\right)+n_{z,i} \end{aligned} \tag{8}$$

where $\left(\hat{B}_{x,i},\hat{B}_{y,i},\hat{B}_{z,i}\right)$ is the set of magnetic flux density values measured by sensor i ($i = 1, \ldots, N$), $\left(B_{x,i},B_{y,i},B_{z,i}\right)$ is the set of real magnetic flux density values (as expressed by (3)-(5) above) and $\left(n_{x,i},n_{y,i},n_{z,i}\right)$ are the set of independent, identically distributed (i.i.d) zero-mean Gaussian random variables with standard deviation σ, which model the measurement noise associated with sensor i. The i.i.d. assumption is one that is usually used in order to come up with results that are analytically tractable. It is certainly possible that in the case of wearable sensors, the sensor noise could be correlated Gaussian (a scenario briefly considered in Appendix B), or even non-Gaussian. For the case of non-Gaussian noise, other distributions, such as Gaussian Mixture Models (GMMs), could be used[31].

Equation (8) can be succinctly written in vector notation as

$$\hat{\mathbf{B}}\left(\varepsilon\right)=\mathbf{B}\left(\varepsilon\right)+\mathbf{n} \tag{9}$$

Therefore, the conditional distribution of the observation vector, $\hat{\mathbf{B}}$, conditioned on the unknown parameter set can be written as

$$p\left(\hat{\mathbf{B}}\middle|\varepsilon\right)=p_n\left(\hat{\mathbf{B}}-\mathbf{B}\right) \tag{10}$$

where $p_n\left(\mathbf{x}\right)$ is the multivariate normal distribution, with mean $\boldsymbol{\mu}$ and covariance $\boldsymbol{\Sigma}$ given by

$$p_n\left(\mathbf{x}\right)=\frac{1}{\left[\left(2\pi\right)^K\det\left(\boldsymbol{\Sigma}\right)\right]^{1/2}}\exp\left[-\frac{1}{2}\left(\mathbf{x}-\boldsymbol{\mu}\right)^T\boldsymbol{\Sigma}^{-1}\left(\mathbf{x}-\boldsymbol{\mu}\right)\right] \tag{11}$$

With the above framework in place, the (j,k) element of the Fisher information matrix can be expressed as (see Appendix A for the derivation)

$$\left[\mathbf{J}_{\varepsilon}\right]_{jk} = \frac{1}{\sigma^2}\sum_{i=1}^{N}V_{jk}^{(i)} \tag{12}$$

where

$$V_{jk}^{(i)} = \frac{\partial B_{x,i}}{\partial \varepsilon_j}\frac{\partial B_{x,i}}{\partial \varepsilon_k}+\frac{\partial B_{y,i}}{\partial \varepsilon_j}\frac{\partial B_{y,i}}{\partial \varepsilon_k}+\frac{\partial B_{z,i}}{\partial \varepsilon_j}\frac{\partial B_{z,i}}{\partial \varepsilon_k} \tag{13}$$

The Fisher matrix is symmetric and can be expressed as a 2×2 block matrix of the form

$$\mathbf{J}_{\varepsilon} = \begin{bmatrix} \mathbf{J}_L & \mathbf{C}_{LO} \\ \mathbf{C}_{LO}^T & \mathbf{J}_O \end{bmatrix} \tag{14}$$

where $\mathbf{J}_L$ and $\mathbf{J}_O$ are 3×3 matrices consisting only of the terms pertaining to the location parameters, (a,b,c), and the orientation parameters, (m,n,p), respectively, as given by

$$\mathbf{J}_L = \begin{bmatrix} J_{aa} & J_{ab} & J_{ac} \\ J_{ba} & J_{bb} & J_{bc} \\ J_{ca} & J_{cb} & J_{cc} \end{bmatrix} \tag{15}$$

$$\mathbf{J}_O = \begin{bmatrix} J_{mm} & J_{mn} & J_{mp} \\ J_{nm} & J_{nn} & J_{np} \\ J_{pm} & J_{pn} & J_{pp} \end{bmatrix} \tag{16}$$

and $\mathbf{C}_{LO}$ is another 3×3 matrix that contains cross-terms between the location and orientation parameters:

$$\mathbf{C}_{LO} = \begin{bmatrix} J_{am} & J_{an} & J_{ap} \\ J_{bm} & J_{bn} & J_{bp} \\ J_{cm} & J_{cn} & J_{cp} \end{bmatrix} \tag{17}$$

Since $\mathbf{J}_{\varepsilon}$ can be written as a block matrix in the form of (11), its inverse will also be a symmetric matrix of the form (for details, see, for example[32])

$$\mathbf{J}_{\varepsilon}^{-1} = \begin{bmatrix} \mathbf{M}_{11} & \mathbf{M}_{12} \\ \mathbf{M}_{12}^T & \mathbf{M}_{22} \end{bmatrix} \tag{18}$$

and since $\mathbf{J}_{\varepsilon}\mathbf{J}_{\varepsilon}^{-1} = \mathbf{I}$, it can be shown that

$$\mathbf{M}_{11} = \left[\mathbf{J}_L - \mathbf{C}_{LO}\mathbf{J}_O^{-1}\mathbf{C}_{LO}^T\right]^{-1} \tag{19}$$

$$\mathbf{M}_{12} = -\mathbf{J}_L^{-1}\mathbf{C}_{LO}\left[\mathbf{J}_O - \mathbf{C}_{LO}^T\mathbf{J}_L^{-1}\mathbf{C}_{LO}\right]^{-1} \tag{20}$$

$$\mathbf{M}_{12}^T = -\mathbf{J}_O^{-1}\mathbf{C}_{LO}^T\left[\mathbf{J}_L - \mathbf{C}_{LO}\mathbf{J}_O^{-1}\mathbf{C}_{LO}^T\right]^{-1} \tag{21}$$

$$\mathbf{M}_{22} = \left[\mathbf{J}_O - \mathbf{C}_{LO}^T\mathbf{J}_L^{-1}\mathbf{C}_{LO}\right]^{-1} \tag{22}$$

Thus, the CRLB is defined only under the assumption that the associated inverses in (19) - (22) are defined.

A close examination of (18) - (22) offers several points of insight. First, the $\mathbf{M}_{11}$ block on the right-hand side of (18) gives the lower bound on error covariance associated with estimation of the *location parameters only*. However, a closer examination of the right-hand side of (19) reveals that this block is affected by the unknown orientation parameters, as evidenced by the presence of terms involving $\mathbf{J}_O$ and $\mathbf{C}_{LO}$. If the orientation parameters, (m,n,p), were somehow known, and the only unknown parameters being estimated were the location parameters (a,b,c), then we would have $\mathbf{M}_{11} = \mathbf{J}_L^{-1}$. Thus, the term $\mathbf{C}_{LO}\mathbf{J}_O^{-1}\mathbf{C}_{LO}^T$ in (19) can be viewed as an objective measure of the "penalty" we have to pay for estimating the location and orientation parameters at the same time. A similar argument can be made regarding the $\mathbf{M}_{22}$ block in (18), which concerns the lower bound associated with estimation of *orientation parameters only*; thus the term $\mathbf{C}_{LO}^T\mathbf{J}_L^{-1}\mathbf{C}_{LO}$ in (22) can be viewed as a measure of the penalty in this case.

A well-known and commonly used metric for evaluating the performance of localization systems is the *Root Mean Square Error* (*RMSE*) which is defined as the square-root of the mean-square error between the estimated and actual location (or orientation) parameters. Thus, a lower-bound on this metric would be of practical interest. Upon examination of (18) – (22), it is clear that the diagonal elements of the $\mathbf{M}_{11}$ block in (18) are the lower-bounds on the error covariance associated with the estimation of location parameters, (a,b,c). Thus a lower-bound on the RMSE for location estimation, denoted by $RMSE_L$, can be calculated based on the sum of the diagonal elements of $\mathbf{M}_{11}$:

$$RMSE_L = \sqrt{sum\left(diag\left(\mathbf{M}_{11}\right)\right)} \tag{23}$$

Similarly, a lower bound on the RMSE for estimation of orientation parameters, denoted by $RMSE_O$, can be determined based on the sum of the diagonal elements of $\mathbf{M}_{22}$:

$$RMSE_O = \sqrt{sum\left(diag\left(\mathbf{M}_{22}\right)\right)} \tag{24}$$

3. RESULTS AND DISCUSSION

In this section, we present and analyze the CRLB results for the magnetic localization technique with real position and orientation values based on a 3-D human body model. We begin with a discussion of the general assumptions underlying the results in the following subsections.

The magnetic localization technique consists of a magnetic source and the sensor plane in which the magnetic sensors are placed. It is assumed that the magnetic source is hollow cylindrical in such a way that it wraps around the outside of the capsule, as shown in Fig. 2. The magnet material is assumed to be NdFeB (Neodymium-Iron-Boron), since this is the material combination with the highest amount of magnetic flux per unit volume. For the purposes of the current study, the geometrical parameters of the magnet are: outer diameter R2=15 mm, inner diameter R1= 11mm, and length L=20 mm with a uniform magnetization value of $M_0 = 750x10^3$ (Amp/meter). The magnetic sensor model is based on Honeywell's (HMC1043) tri-axial magnetic field sensors. For the purposes of this analysis, the sensor array on the body surface was created by taking into the account 3-dimensional human body dimensioning the model. Fig. 3 (a), (b) and (c) show the body model where the sensors are placed, the tissue state of the intestine in this body, the shape of the intestine transformed into a digital solid model to obtain the capsule positions, respectively. Solidworks™ CAD software was used to obtain the digital 3-D model of the intestinal region and an interpolation relationship was defined between known real intestinal positions. The goal here is to create a framework for performance evaluation which would allow for numerical evaluation of the CRLB at an arbitrary number of positions in the large as well as the small intestine.

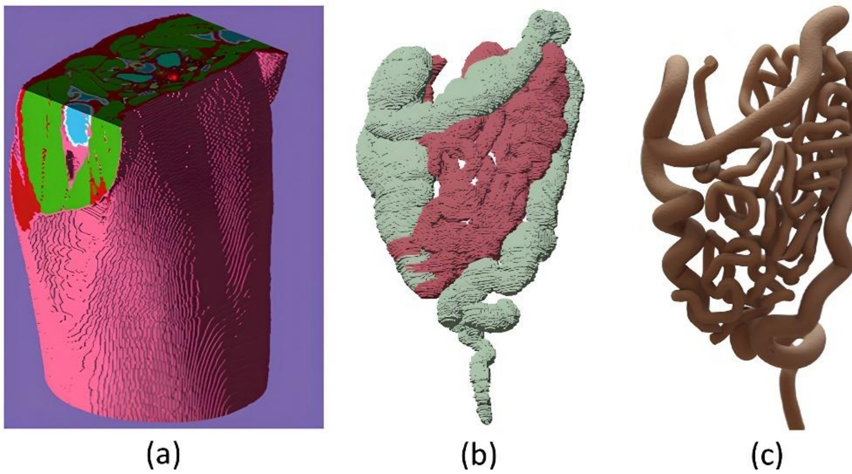

Figure 3. (a) Human torso model, (b) Intestine tissue model, (c) Numerical intestine model

A total of 256 magnetic sensors in contact with the skin are used on the body model. In addition, simulation data were obtained for 375 locations in which the magnetic capsule was positioned in the intestine model. The entire 3D working space, where the sensor and capsule positions can be seen together, is given in Fig. 4.

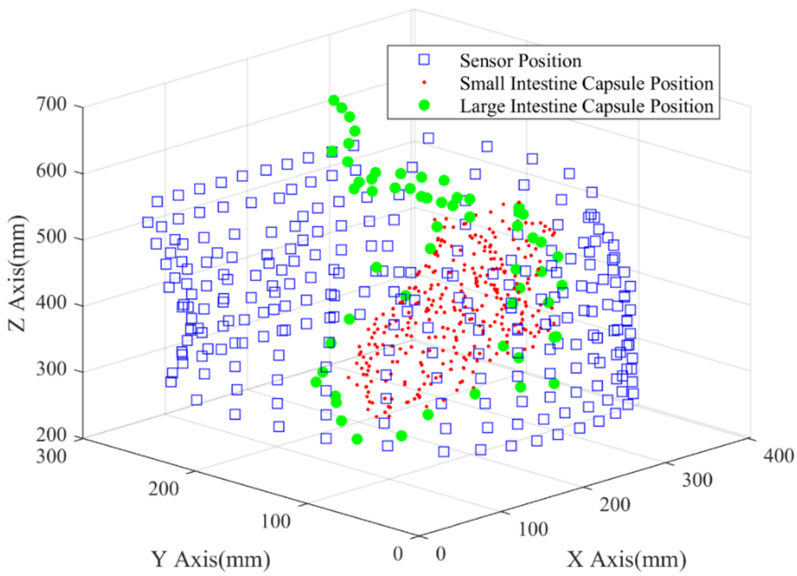

Figure 4. Sensor and capsule locations

3.1 *CRLB for Capsule Position and Orientation Parameters*

CRLB values are shown in Fig. 5 and Fig. 6 according to the increase in the number of sensors for each position in the capsule movement. The results reported here are based on 375 positions of the capsule covering the small intestine and large intestine. These results are a function of the number of sensors, which was increased to a maximum of 256. Fig. 5 shows the CRLB values for the capsule's position parameters, while Fig. 6 shows CRLB values for the capsule's orientation parameters. CRLB values above average are observed in capsule positions in the large intestine (318-375) and in the small intestine (1-317). When examining Fig. 5 and Fig.6 for each position during the capsule's movement, it is observed that the maximum CRLB values occur in the 4-sensor configuration, while the CRLB values progressively decrease in the 8 and 16 sensor configurations. Although the CRLB values between these three sensor configurations are noticeable, the difference decreases and CRLB values are minimized when the effects of 32 and 64 sensor configurations are analyzed. In the subsequent 128 and 256 sensor configurations, no substantial change in CRLB values is observed.

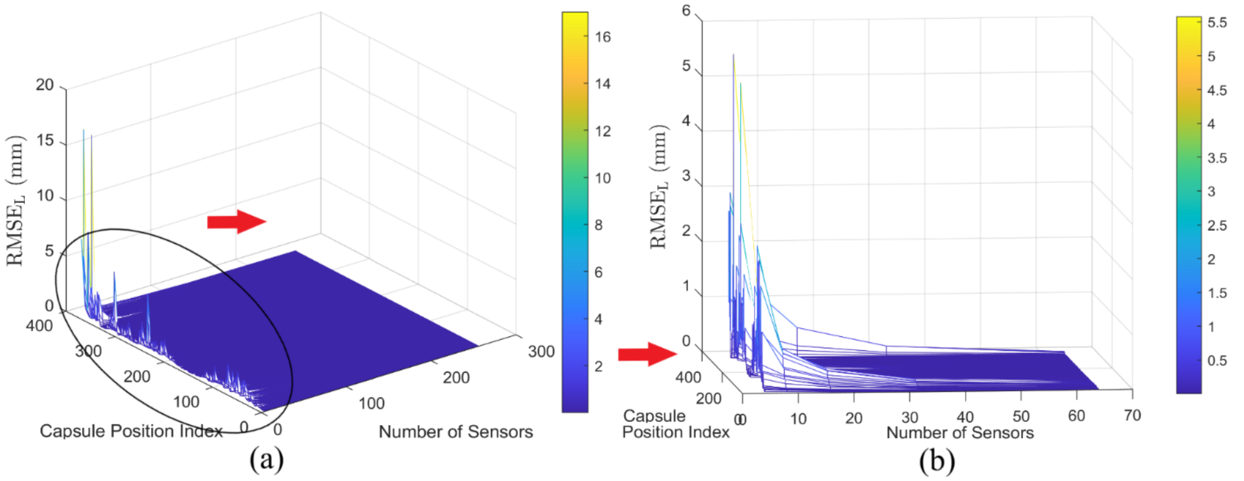

Figure 5. (a) RMSEL for capsule position parameters (b) zoomed region

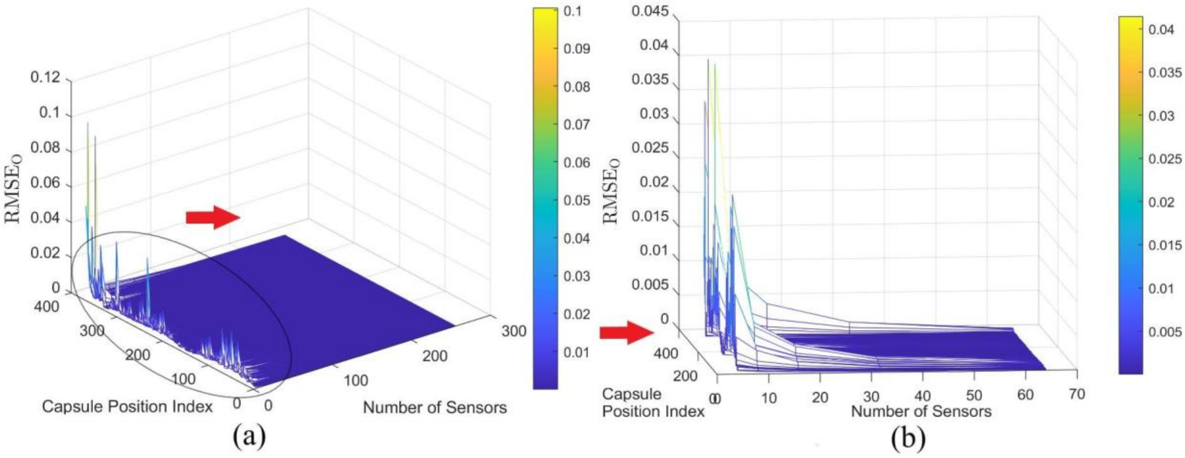

Figure 6. (a) RMSEO for capsule orientation parameters (b) zoomed region

By averaging the values across each capsule position, Fig. 7 is generated. This figure illustrates how increasing the sensor count leads to a reduction in the average RMSE values. Specifically, when the sensor configuration is increased from 4 to 8 sensors, the average RMSE value decreases by 82.79%. This reduction further improves to 91.43% when the sensor count is raised to 16. Similarly, a 32-sensor array achieves a 96.53% decrease in total error compared to a 4-sensor configuration, while a 64-sensor array shows a reduction of 98.98%. This ratio decreases to a minimum in arrays with 128 and 256 sensors. Fig. 7(b) presents data for sensor arrays ranging from 32 to 64 sensors. When evaluating the RMSE reduction for every 8-sensor increase, a 31.63% improvement is observed between 32 and 40 sensors, which further increases to 50.87% at 48 sensors. In contrast, further additions to 56 and 64 sensors yield only an approximate 10% reduction. Based on these results, it can be concluded that a 48-sensor array achieves an optimal balance between the sensor count and RMSE error reduction.

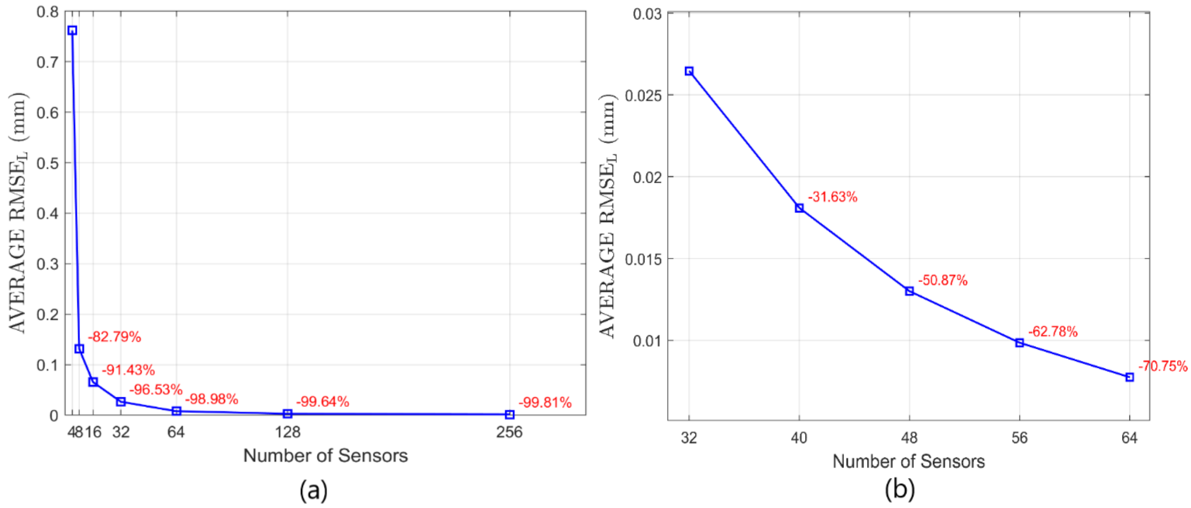

Figure 7. (a) Average RMSE$_L$ for capsule position parameters (b) between 32 and 64 sensors

3.2 *Effect of Magnet Size on CRLB*

In this section, we examine the effect of the size of the magnet wrapped outside the capsule on the CRLB. An attempt has been made to find out how the thickness and length of the magnet affect the CRLB. Fig. 8 shows CRLB values according to the increase in the number of sensors for different magnet sizes and thicknesses. The CRLB values presented here are average values, based on CRLB values obtained at all capsule locations (375 in total). The graph is based on an estimate of the capsule's position parameters. The number of sensors is again gradually increased up to a maximum of 256 sensors. In the results, it is seen that increasing the size of the magnet reduces CRLB values by the same rate. This, in turn, can be explained by the fact that the increase in the size of the magnet is directly proportional to the increase in the magnetic field.

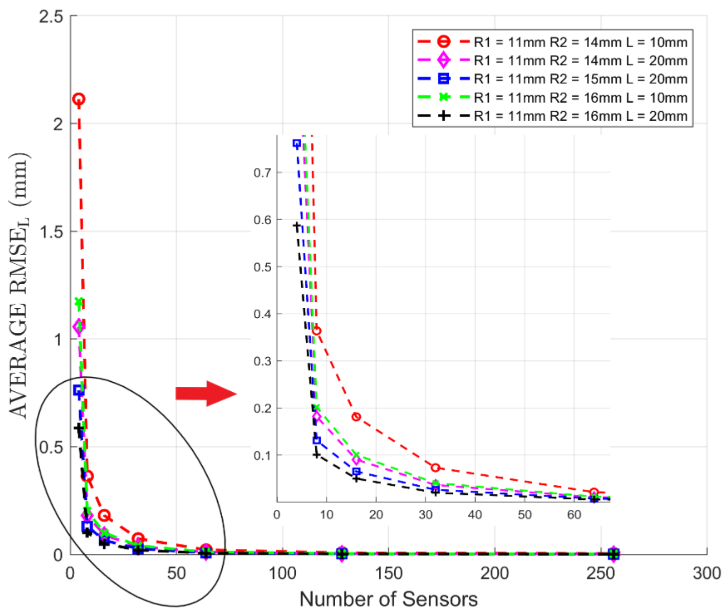

Figure 8. RMSE by magnet size

Increasing the size of the magnet can create practical limitations, as it increases the overall dimensions of the capsule. Difficulty swallowing, limitations based on bowel size, and discomfort to the patient, are all factors that should be considered when determining the size of the magnet. A review of the medical literature compares the dimensions of some of the most widely used capsule endoscope devices [33]. Based on this information, the average length of the device appears (end-to-end, including the dome-shaped cameras, potentially at both ends) to be approximately 25.5 mm and the average diameter is approximately 11 mm. Considering the cylindrical structure of the magnet as shown in Fig. 2, it is obvious that the length of the magnet needs to be less than 25.5 mm (since the field-of-view of the camera should not be obstructed). Therefore, a length of L = 20 mm is reasonable. The CRLB values for two different values of L, and different thickness values (i.e. different values of R2) are shown in Fig. 8. Of particular interest from this perspective, is the case where L = 20 mm and R2 = 14 mm (see purple curve on Fig. 8). This particular scenario translates to a magnet thickness of only 1.5 mm and thus can be considered practically feasible. Thus, the results of Fig. 8 clearly show that highly accurate localization is possible at practically feasible magnet dimensions.

3.3 *Effect of the Magnetic Material on the CRLB*

The size of the magnet, as well as the type of magnetic material, affects the magnetic field of the magnet, and thus the CRLB. In this study, the effect of different types of magnets with different uniform magnetism values on CRLB was examined. The goal here is to determine which type of magnet will give better localization performance. The magnet types considered are FeCoCr, Alnico, Ferrite, SmCo and NdFeB. These magnets are the main hard magnetic materials[34]. The graph in Fig. 9 is obtained when magnets are compared according to uniform magnetism values. The graph is based on estimate of the capsule's position parameters, and CRLB is an average of the capsule positions. As can be seen from the graph, the increase in uniform magnetism gives lower CRLB values. NdFeB and SmCo magnets appear to give the smallest CRLB values with the highest uniform magnetism values, indicating that these are the best magnetic materials for optimal positioning performance. The results of Fig. 9 also clearly illustrate that after a certain number of sensors (approximately 50), the graph becomes flat, indicating that it really does not matter which magnetic material is used. This observation can be explained by the notion that if the system employs a relatively large number of magnetic sensors, a certain subset will be able to provide measurements of high enough quality (enough to compensate for those sensors with lower-quality measurements) so that the overall localization performance will not be impacted noticeably.

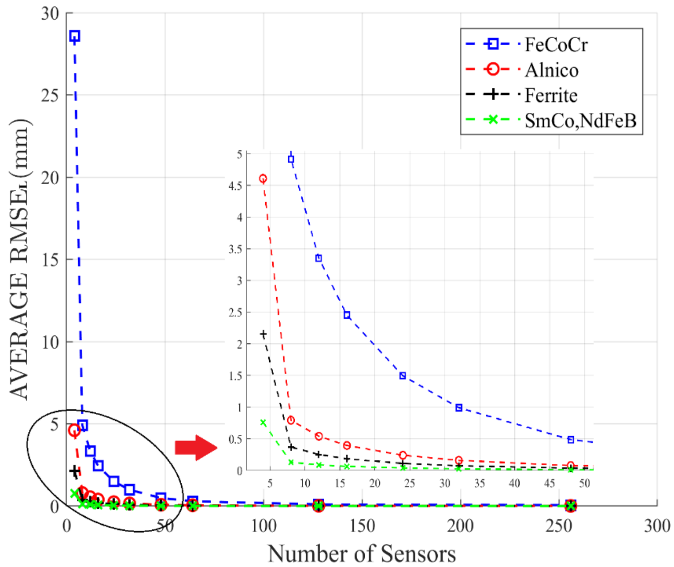

Figure 9. RMSE by uniform magnetism value

3.4 *Effect of Sensor Location on CRLB*

It is to be expected that the localization performance (and thus the CRLB) will be affected by the location of the sensors on the body surface. With this in mind, , localization performance is compared on the basis of the CRLB according to the body region where the sensors are employed. 48 sensors were selected for the four separate regions of the body surface (denoted as "left", "right", "front" and "back" in the results that follow), as shown in Figure 10.

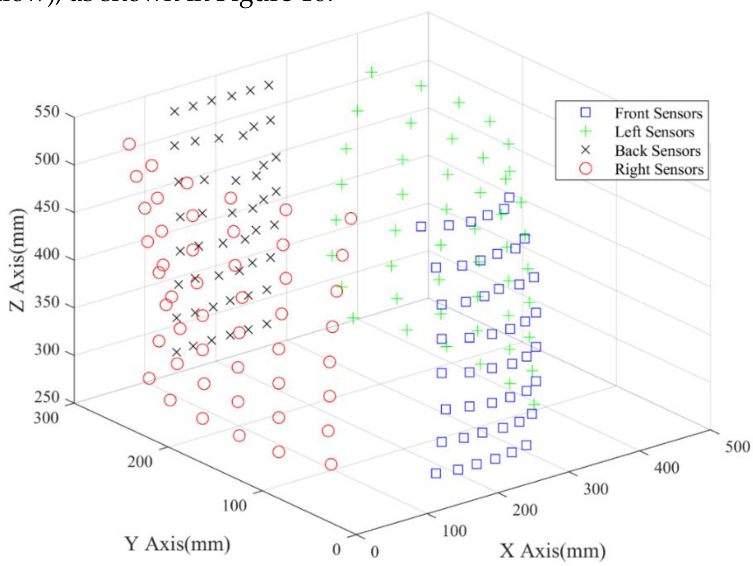

Figure 10. 48 sensor locations selected for each body part

The question here is: which of these four regions of the body would give rise to better localization performance (i.e. lower localization and orientation error)? show CRLB values for position and orientation parameters (based on the region where the sensors are employed) relative to actual capsule positions in the GI tract.

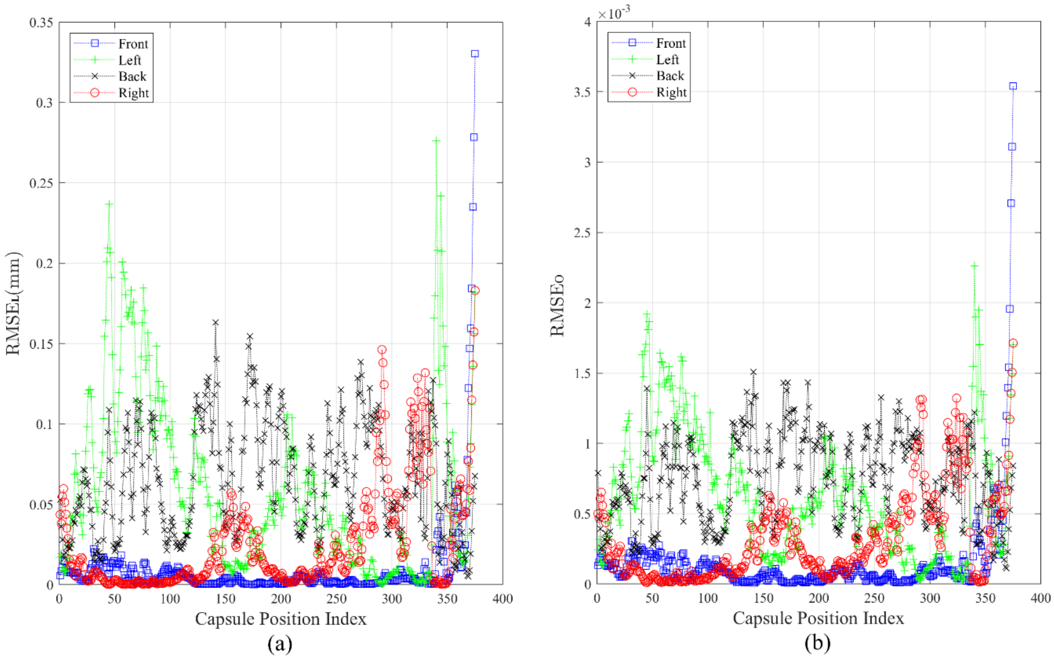

Figure 11. (a) RMSE$_L$ for position parameters by body region, (b) RMSE$_O$ for orientation parameters by body region

In order to give a more simplified view of the above results, Table I gives CRLB values averaged over all capsule positions for the four separate regions. Based on these results, it is seen that the smallest estimation error can be achieved with sensors placed on the front region of the body (covering the torso), indicating that that is the region of the body surface for optimal localization performance. This might well have to do with the fact that the intestinal region, in general, is closer to the front surface of the body (i.e. the torso) as opposed to the back of the body, thus allowing higher-quality magnetic sensor data. The right part of the body resulted in the second lowest prediction error, while the left and back part gave an equal prediction error. To illustrate this point another way, a 3-D intestinal "heat map" of the CRLB values is shown for the four sensor regions in Fig. 12.

Table 1 Average RMSE by Capsule Location

RMSE	**Front**	**Back**	**Left**	**Right**
Position (mm)	0.0098	0.0656	0.0593	0.0246
Orientation (10^{-4})	1.4791	7.3919	6.3185	3.1047

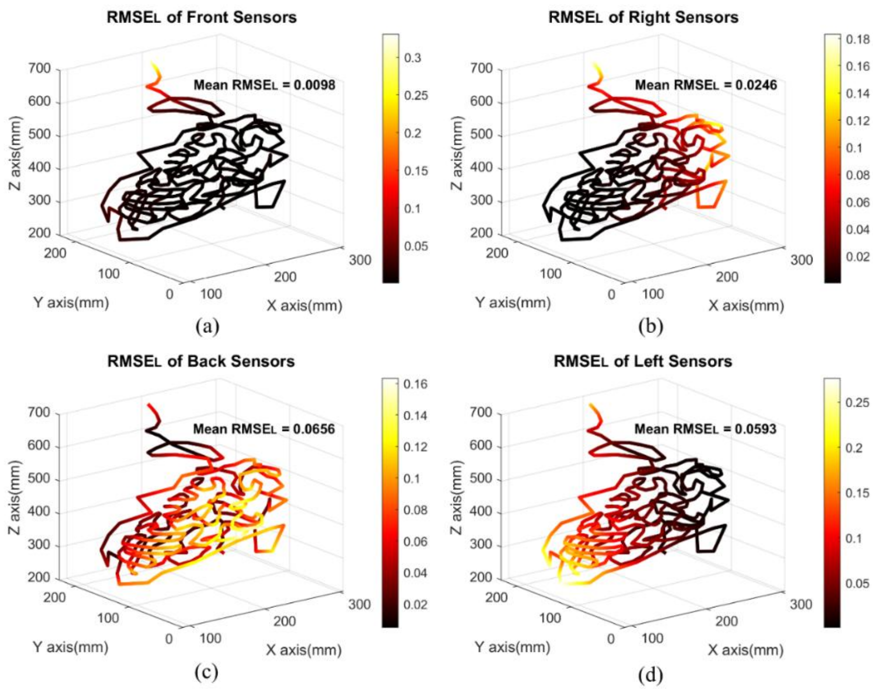

Figure 12. Intestinal heat map of $RMSE_L$ values according to sensor position on the body (a)Front Sensors (b) Right Sensors (c) Back Sensors (d)Left Sensors

The results, as given in Fig. 12, show that localization performance with the front placement of sensors, while satisfactory in some parts of the intestine, is not quite as good in other parts. This raises yet another question: is it possible to enhance performance by providing spatial diversity among sensors? In other words, is it possible to enhance localization performance by augmenting the sensors placed on the front with sensors placed on the left and the right? The next set of results attempt to answer these questions. The sensor locations on the body surface for this study are shown in Fig. 13. In order to facilitate an effective comparison with the previous set of results, the total number of sensors is kept fixed at 48; however, 24 of these are located on the front of the torso, and the rest are located either on the right or the left. Note that the case of sensors on the back of the torso was not incorporated into this particular set of results, since the results of Fig. 14 clearly indicate poorer localization performance in this case.

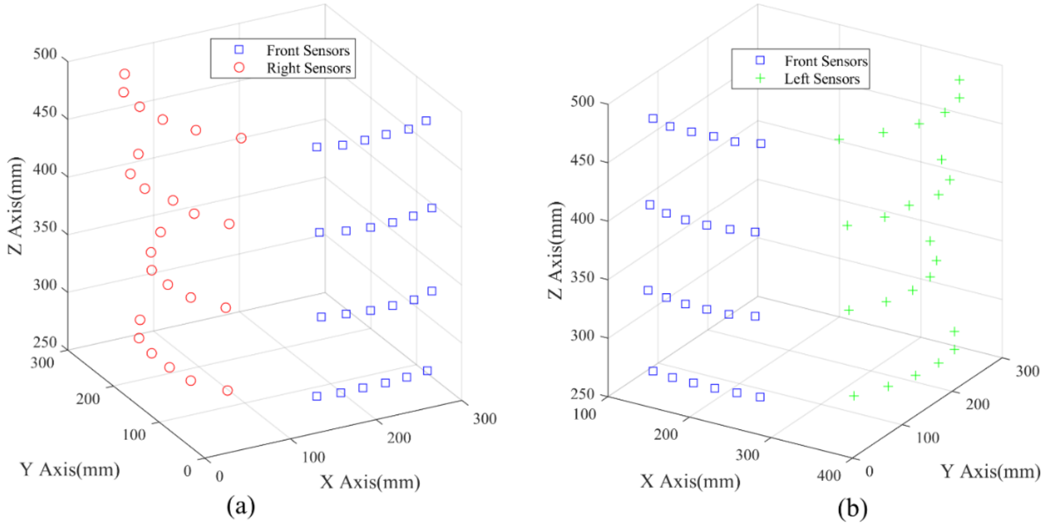

Figure 13. (a) Front and Right sensors locations (b) Front and Left sensors locations

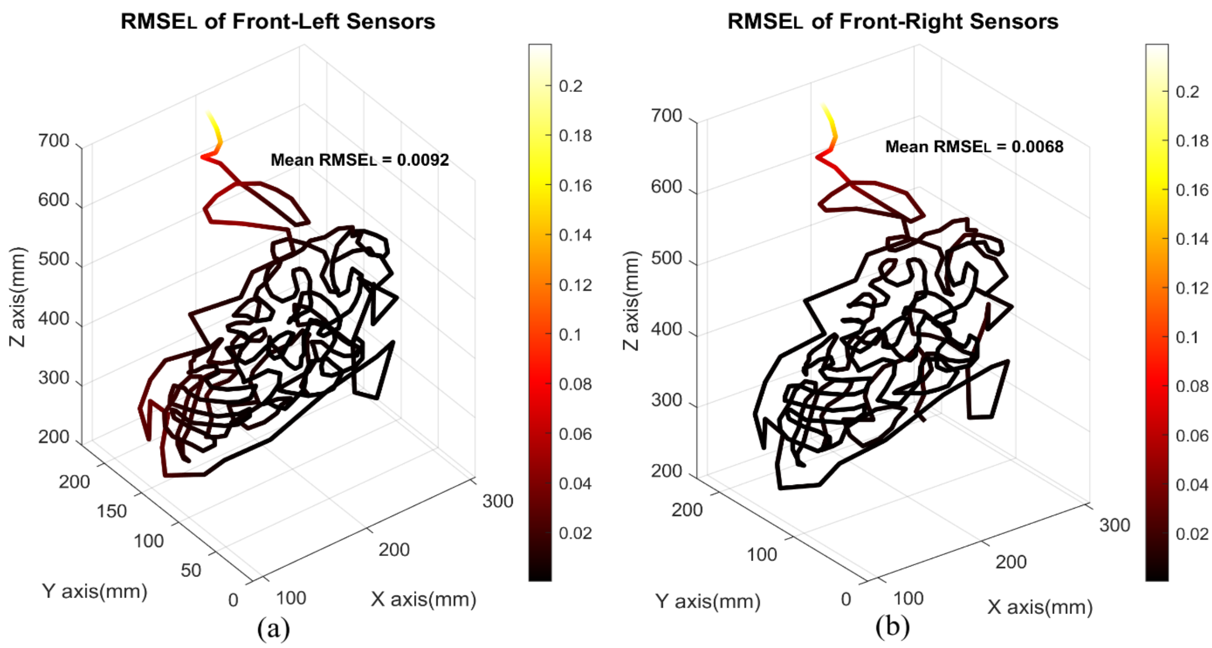

Figure 14. The impact of spatial diversity among sensors: Intestinal heat map of localization RMSE values based on the location of sensors: (a) Front-Left (b) Front-Right

Once again, in order to convey a more simplified perspective on the above results, the average RMSE over all the capsule locations considered in Fig. 14 has been computed and tabulated in Table II. These results show that, on average, both the positioning and orientation RMSE figures for the front-right case are approximately 26% better than the corresponding figures for the front-left case. To interpret these results in another way, we can compare the average RMSE figures for the ***front-right*** case to the results for the ***front*** case in Table I. This comparison indicates that the average positioning RMSE for the front-right case is approximately 31% better than the figure for the front case. A similar comparison for the average orientation RMSE indicates that the front-right case results in a performance improvement of approximately 30%. These results indicate that spatial diversity among sensors can have a positive impact on performance.

Table 2 Average RMSE by Capsule Location (Spatial Diversity Case)

RMSE	Front-Left	Front-Right
Position (mm)	0,0092	0,0068
Orientation (10^{-4})	1,3986	1,0405

3.5 General Discussion

Some general points pertaining to the above results are worthy of further discussion. The first such point involves the 3D body model used to derive the results.

The results reported in this paper are based on one 3D body model, the details of which are publicly available. It is a fact that no two human bodies are exactly alike. There are differences in body mass index, patient size and body composition (e.g. the amount of muscle versus fat). In addition, there are dynamic factors, such as bowel movements, which can cause subtle changes in the position of the organs in the GI tract. All of these factors can affect the magnetic field distribution, and thus the CRLB, and cannot necessarily be accounted for in a static 3-D model. The ideal way to address this issue would be to compute the CRLB for a number of different body models of adequate resolution; unfortunately, at the time of writing, the authors only had access to a single body model which satisfied this criterion.

In lieu of computing the CRLB for a range of body models, a small-scale sensitivity analysis is attempted, and the results are depicted in Fig. 15. This analysis is based on the 48 sensors located on the torso region. In this analysis, we have attempted to assess how the CRLB changes as a function of patient size in the torso region (as might be the case, for example, for a patient with a greater or lesser amount of body fat in the torso, compared to the original body model). This was simulated by adding or subtracting an offset value (20 mm) from the y-coordinate of all the sensors, and the resulting change in the CRLB values are shown in Fig. 15. It is observed that when the offset value is added, meaning the sensors are positioned farther from the body, the RMSE values increase; whereas when the offset value is subtracted, meaning the sensors are positioned closer to the body, the RMSE values decrease. In part (b) of Figure 15, a zoomed-in view is presented, and the mentioned differences can be clearly observed. These results show, at least at a basic level, that increases in patient size in the torso region could increase CRLB values.

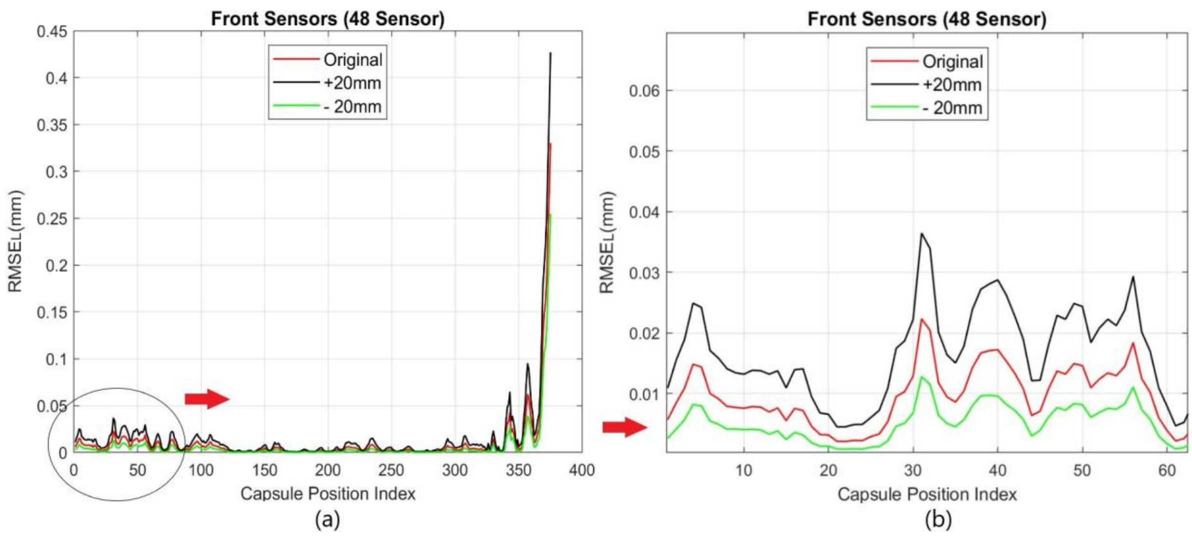

Figure 15. (a) RMSE by sensor distance (b) zoomed region

The second point worthy of discussion involves real-time localization of the capsule for RCE applications. Since CRLB represents a lower bound on the accuracy of a location estimator, it does not specify how real-time localization might be implemented. Nevertheless, the ability to accurately localize the capsule inside the body in a short timeframe is critical for RCE applications. The basic idea behind the localization algorithms is to leverage an analytical model for the magnetic field distribution (such as the dipole model of equation (1)) to solve an inverse problem, i.e. to find the location coordinates (a,b,c) and the orientation parameters (m,n,p). Since the analytical models are inherently nonlinear functions of the location and orientation parameters, optimization methods are generally used to solve the problem. One very commonly used algorithm is the Levenberg-Marquardt (L-M) algorithm [35]. This algorithm, however, is generally very sensitive to the starting point for the calculations, and can take a long time to converge. To speed up the convergence, the L-M algorithm is generally used in conjunction with a metaheuristics algorithm, which can both provide a good starting point, thus speeding up convergence [16].

4 CONCLUSION

In this paper, we focused on the problem of magnetic localization for wireless capsule endoscopy, and specifically attempted to address the question of optimal performance through the use of the Cramer-Rao Lower Bound (CRLB). In order to obtain results of practical significance, a realistic 3-D human body model is used. Various scenarios have been considered with different sensor configurations and other system-related parameters, such as magnet size and magnetic materials. Based on the results obtained, we conclude that there is an optimal number of sensors (which appears to be 48), beyond which no appreciable improvement in the performance is obtained and that sensors should be positioned on the front of the body for optimal performance. The results also indicate that there are tradeoffs that need to be made in terms of magnetic materials and magnet size and their impact on performance. We believe the results should be of interest to all scientists and engineers interested in advancing wireless capsule endoscopy. Future work will focus on different cases for measurement noise and comparison of the results with other localization methods and practical testbed scenarios.

Declaration of Ethical Standards

The authors declare that the study complies with all applicable laws and regulations and meets ethical standards.

Credit Authorship Contribution Statement

Author 1: Methodology, Supervision, Validation, Formal analysis, Writing – review & editing
Author 2: Conceptualization, Formal analysis, Investigation, Methodology, Resources, Software, Writing – original draft, Writing – review & editing,
Author 3: Formal analysis, Investigation, Resources, Visualization, Writing – review & editing,

Declaration of Competing Interest

The authors declare that they have no known competing financial interests or personal relationships that could have appeared to influence the work reported in this paper.

Funding / Acknowledgements

The authors acknowledge that no funding support has been sought for the work reported in this paper, and thank the anonymous reviewers for their help and thoughtful comments.

Data Availability

The data that support the findings of this study are available from the corresponding author upon reasonable request.

REFERENCES

[1] G. Iddan, G. Meron, and A. Glukhovsky, "Wireless capsule endoscopy. Nature," *vol,* vol. 405, p. 25, 2000.

[2] G. J. Iddan and C. P. Swain, "History and development of capsule endoscopy," *Gastrointestinal Endoscopy Clinics,* vol. 14, no. 1, pp. 1-9, 2004.

[3] M. Kanaan and H. Farhadi, "Advances in wireless video capsule endoscopy," *International Journal of Wireless Information Networks,* vol. 24, pp. 166-167, 2017.

[4] B. S. Lewis and P. Swain, "Capsule endoscopy in the evaluation of patients with suspected small intestinal bleeding: results of a pilot study," *Gastrointestinal endoscopy,* vol. 56, no. 3, pp. 349-353, 2002.

[5] O. H. Maghsoudi, M. Alizadeh, and M. Mirmomen, "A computer aided method to detect bleeding, tumor, and disease regions in Wireless Capsule Endoscopy," in *2016 IEEE Signal Processing in Medicine and Biology Symposium (SPMB)*, 2016: IEEE, pp. 1-6.

[6] X. Wang, *Study on magnetic localization and actuation of active capsule endoscope* (no. 03). 2006.

[7] T. D. Than, G. Alici, H. Zhou, and W. Li, "A review of localization systems for robotic endoscopic capsules," *IEEE transactions on biomedical engineering,* vol. 59, no. 9, pp. 2387-2399, 2012.

[8] A. Moglia, A. Menciassi, M. O. Schurr, and P. Dario, "Wireless capsule endoscopy: from diagnostic devices to multipurpose robotic systems," *Biomedical microdevices,* vol. 9, no. 2, pp. 235-243, 2007.

[9] G. Ciuti, A. Menciassi, and P. Dario, "Capsule endoscopy: from current achievements to open challenges," *IEEE reviews in biomedical engineering,* vol. 4, pp. 59-72, 2011.

[10] D. Fischer, R. Schreiber, D. Levi, and R. Eliakim, "Capsule endoscopy: the localization system," *Gastrointestinal Endoscopy Clinics,* vol. 14, no. 1, pp. 25-31, 2004.

[11] C. Hu, M. Q.-H. Meng, and M. Mandal, "Efficient magnetic localization and orientation technique for capsule endoscopy," *International Journal of Information Acquisition,* vol. 2, no. 01, pp. 23-36, 2005.

[12] C. Xiao, Z. Liang, and J. Yang, "Radiation characteristic analysis of antenna deeply implanted in human body and localization sensor array," *IEEE Transactions on Instrumentation and Measurement,* vol. 71, pp. 1-12, 2022.

[13] K. Diamantis, T. Anderson, J. A. Jensen, P. A. Dalgarno, and V. Sboros, "Development of super-resolution sharpness-based axial localization for Ultrasound Imaging," *IEEE Access,* vol. 7, pp. 6297-6309, 2018.

[14] J. Boese, N. Rahn, and B. Sandkamp, "Method for determining the position and orientation of an object, especially of a catheter, from two-dimensional X-ray images," ed: Google Patents, 2010.

[15] P. Muruganantham and S. M. Balakrishnan, "Attention aware deep learning model for wireless capsule endoscopy lesion classification and localization," *Journal of Medical and Biological Engineering,* vol. 42, no. 2, pp. 157-168, 2022.

[16] M. Suveren, R. Akay, M. Y. Yildirim, and M. Kanaan, "Application of hybrid metaheuristic with Levenberg-Marquardt algorithm for 6-dimensional magnetic localization," *Evolving Systems,* vol. 13, no. 6, pp. 849-867, 2022.

[17] I. Castro, J. W. de Wit, J. van Vooren, T. Van Quaethem, W. Huang, and T. Torfs, "Magnetic localization of wireless ingestible capsules using a belt-shaped array transmitter," *Electronics,* vol. 12, no. 10, p. 2217, 2023.

[18] A. C. Moldovan, M. V. Turcanu, S. Mitra, and S. Cochran, "Ultrasound technology for capsule endoscopy," in *Endorobotics*: Elsevier, 2022, pp. 215-240.

[19] N. Pagoulatos, W. S. Edwards, D. R. Haynor, and Y. Kim, "Interactive 3D registration of ultrasound and magnetic resonance images based on a magnetic position sensor," *IEEE Transactions on Information Technology in Biomedicine,* vol. 3, no. 4, pp. 278-288, 1999.

[20] T. D. Than *et al.*, "An effective localization method for robotic endoscopic capsules using multiple positron emission markers," *IEEE Transactions on Robotics,* vol. 30, no. 5, pp. 1174-1186, 2014.

[21] F. Bianchi *et al.*, "Localization strategies for robotic endoscopic capsules: a review," *Expert review of medical devices,* vol. 16, no. 5, pp. 381-403, 2019.

[22] B. Moussakhani, T. Ramstad, J. T. Flåm, and I. Balasingham, "On localizing a capsule endoscope using magnetic sensors," in *2012 Annual International Conference of the IEEE Engineering in Medicine and Biology Society*, 2012: IEEE, pp. 4058-4062.
[23] M. N. Sadiku *et al.*, *Fundamentals of engineering electromagnetics*. CRC press, 2018.
[24] F. T. Ulaby and U. Ravaioli, *Fundamentals of applied electromagnetics*. Pearson Upper Saddle River, NJ, 2015.
[25] H. L. Van Trees, *Detection, estimation, and modulation theory, part I: detection, estimation, and linear modulation theory*. John Wiley & Sons, 2004.
[26] A. Eshkevari and S. M. S. Sadough, "On the Cramer-Rao Lower Bound Based Analysis of Direct Position Determination and DOA Position Finding for Co-Channel Emitter Localization," *Journal of Applied Research in Electrical Engineering,* vol. 1, no. 2, pp. 131-138, 2022.
[27] D. Dmitrieva, D. Anzai, J. Kirchner, G. Fischer, and J. Wang, "Cost-Efficient Real-Time Adaptive Location Tracking With Interacting Multiple Transition Model for Implantable Medical Device," *IEEE Journal of Electromagnetics, RF and Microwaves in Medicine and Biology,* vol. 7, no. 2, pp. 102-109, 2022.
[28] A. Eshkevari and S. M. S. Sadough, "An improved method for localization of wireless capsule endoscope using direct position determination," *IEEE Access,* vol. 9, pp. 154563-154577, 2021.
[29] M. Kanaan and M. Cil, "Cramer-Rao Lower Bounds for Magnetic Localization of a Wireless Capsule Endoscope based on the Magnetic Dipole Model," in *2019 IEEE 30th International Symposium on Personal, Indoor and Mobile Radio Communications (PIMRC Workshops)*, 2019: IEEE, pp. 1-5.
[30] A. Dammann, B. Siebler, and S. Sand, "Cramér–Rao Lower Bound for Magnetic Field Localization around Elementary Structures," *Sensors,* vol. 24, no. 8, p. 2402, 2024.
[31] T. Costa, G. Boccignone, and M. Ferraro, "Gaussian mixture model of heart rate variability," *PloS one,* vol. 7, no. 5, p. e37731, 2012.
[32] T.-T. Lu and S.-H. Shiou, "Inverses of 2× 2 block matrices," *Computers & Mathematics with Applications,* vol. 43, no. 1-2, pp. 119-129, 2002.
[33] N. Hosoe, K. Takabayashi, H. Ogata, and T. Kanai, "Capsule endoscopy for small-intestinal disorders: current status," *Digestive Endoscopy,* vol. 31, no. 5, pp. 498-507, 2019.
[34] S. Tumanski, *Handbook of magnetic measurements*. CRC press, 2016.
[35] M. Chi, S. Chang, Z. Guo, Q. Zhao, G. Zhang, and F. Meng, "Research on localization control of magneto-controlled capsule endoscopy based on sensor array," *Robotic Intelligence and Automation,* 2025.
[36] S. M. Kay, "Fundamentals of Statistical Signal Processing: Estimation Theory," ed: Prentice Hall, 1993.
[37] A. Verbyla, "A NOTE ON THE INVERSE COVARIANCE MATRIX OF THE AUTOREGRESSIVE PROCESS 1," *Australian Journal of Statistics,* vol. 27, no. 2, pp. 221-224, 1985.

APPENDIX A – CALCULATION OF THE FISHER MATRIX

The derivation proceeds from equation (10). Since the noise samples are assumed to be zero-mean, i.i.d. with the same variance σ^2, it is clear that $\mathbf{\Sigma} = \sigma^2 \mathbf{I}$,where $\mathbf{I}$ is the identity matrix. Using the identities for inverse and determinant of a diagonal matrix, we can write

$$p\left(\hat{\mathbf{B}} \middle| \boldsymbol{\varepsilon}\right) = \frac{1}{\left[2\pi\sigma^2\right]^{K/2}} \cdot \exp\left[-\frac{1}{2}\left(\hat{\mathbf{B}} - \mathbf{B}\right)^T \mathbf{\Sigma}^{-1} \left(\hat{\mathbf{B}} - \mathbf{B}\right)\right] \tag{A.1}$$

Taking the logarithm of both sides of (A.1) yields

$$\begin{aligned}\log p\left(\hat{\mathbf{B}}\middle|\boldsymbol{\varepsilon}\right) &= \log\frac{1}{\left[2\pi\sigma^2\right]^{K/2}} - \frac{1}{2}\left(\hat{\mathbf{B}}-\mathbf{B}\right)^T \boldsymbol{\Sigma}^{-1}\left(\hat{\mathbf{B}}-\mathbf{B}\right) \\ &= \log\frac{1}{\left[2\pi\sigma^2\right]^{K/2}} - \frac{1}{2\sigma^2}\sum_{i=1}^{N}\left[\left(\hat{B}_{x,i}-B_{x,i}\right)^2 + \left(\hat{B}_{y,i}-B_{y,i}\right)^2 + \left(\hat{B}_{z,i}-B_{z,i}\right)^2\right]\end{aligned} \tag{A.2}$$

Taking the partial derivative of both sides of (A.2), the *jk*-element of the Fisher matrix can be succinctly written as shown in equation (9) above (see[36]). To come up with more succinct expressions below, we let

$$x = x_i - a \tag{A.3}$$

$$y = y_i - b \tag{A.4}$$

$$z = z_i - c \tag{A.5}$$

$$q = mx + ny + pz \tag{A.6}$$

$$R_i = \sqrt{(x_i-a)^2 + (y_i-b)^2 + (z_i-c)^2} \tag{A.7}$$

As such, the expressions for the specific elements of the matrix are based on $V_{jk}^{(i)}$ and can be written as

$$V_{aa}^{(i)} = \frac{9m^2}{R_i^8} + \frac{9q^2 + 9x^2 - 36mqx}{R_i^{10}} + \frac{45q^2x^2}{R_i^{12}} \tag{A.8}$$

$$V_{bb}^{(i)} = \frac{9n^2}{R_i^8} + \frac{9q^2 + 9y^2 - 36nqy}{R_i^{10}} + \frac{45q^2y^2}{R_i^{12}} \tag{A.9}$$

$$V_{cc}^{(i)} = \frac{9p^2}{R_i^8} + \frac{9q^2 + 9z^2 - 36pqz}{R_i^{10}} + \frac{45q^2z^2}{R_i^{12}} \tag{A.10}$$

$$V_{ab}^{(i)} = V_{ba}^{(i)} = \frac{9mn}{R_i^8} + \frac{9xy - 18q(my+nx)}{R_i^{10}} + \frac{45xyq^2}{R_i^{12}} \tag{A.11}$$

$$V_{ac}^{(i)} = V_{ca}^{(i)} = \frac{9mp}{R_i^8} + \frac{9xz - 18q(mz+px)}{R_i^{10}} + \frac{45xzq^2}{R_i^{12}} \tag{A.12}$$

$$V_{bc}^{(i)} = V_{cb}^{(i)} = \frac{9np}{R_i^8} + \frac{9zy - 18q(nz+py)}{R_i^{10}} + \frac{45yzq^2}{R_i^{12}} \tag{A.13}$$

$$V_{mm}^{(i)} = \frac{3x^2}{R_i^8} + \frac{1}{R_i^6} \tag{A.14}$$

$$V_{nn}^{(i)} = \frac{3y^2}{R_i^8} + \frac{1}{R_i^6} \tag{A.15}$$

$$V_{pp}^{(i)} = \frac{3z^2}{R_i^8} + \frac{1}{R_i^6} \tag{A.16}$$

$$V_{mn}^{(i)} = V_{nm}^{(i)} = \frac{3xy}{R_i^8} \tag{A.17}$$

$$V_{mp}^{(i)} = V_{pm}^{(i)} = \frac{3xz}{R_i^8} \tag{A.18}$$

$$V_{np}^{(i)} = V_{pn}^{(i)} = \frac{3yz}{R_i^8} \tag{A.19}$$

$$V_{am}^{(i)} = V_{ma}^{(i)} = \frac{3(q-mx)}{R_i^8} + \frac{12x^2q}{R_i^{10}} \tag{A.20}$$

$$V_{an}^{(i)} = V_{na}^{(i)} = \frac{3(nx-2my)}{R_i^8} + \frac{12xyq}{R_i^{10}} \tag{A.21}$$

$$V_{ap}^{(i)} = V_{pa}^{(i)} = \frac{3(px-2mz)}{R_i^8} + \frac{12xzq}{R_i^{10}} \tag{A.22}$$

$$V_{bm}^{(i)} = V_{mb}^{(i)} = \frac{3(my-2nz)}{R_i^8} + \frac{12xyq}{R_i^{10}} \tag{A.23}$$

$$V_{bn}^{(i)} = V_{nb}^{(i)} = \frac{3(q-ny)}{R_i^8} + \frac{12y^2q}{R_i^{10}} \tag{A.24}$$

$$V_{bp}^{(i)} = V_{pb}^{(i)} = \frac{3(py-2nz)}{R_i^8} + \frac{12zyq}{R_i^{10}} \tag{A.25}$$

$$V_{cm}^{(i)} = V_{mc}^{(i)} = \frac{3(mz-2px)}{R_i^8} + \frac{12xzq}{R_i^{10}} \tag{A.26}$$

$$V_{cn}^{(i)} = V_{nc}^{(i)} = \frac{3(nz-2py)}{R_i^8} + \frac{12yzq}{R_i^{10}} \tag{A.27}$$

$$V_{cp}^{(i)} = V_{pc}^{(i)} = \frac{3(q-pz)}{R_i^8} + \frac{12z^2q}{R_i^{10}} \tag{A.28}$$

APPENDIX B – CORRELATED GAUSSIAN NOISE SCENARIO

The correlated Gaussian noise scenario corresponds to the case where the covariance matrix, $\mathbf{\Sigma}$, is not necessarily diagonal, i.e. $\mathbf{\Sigma} \neq \sigma^2\mathbf{I}$. Suppose that the *N* sensor measurements are spatially correlated, i.e. the magnetic flux density components for the *i*-th sensor measurement (*i=1,…,N)* are modeled as an AR(1) random process (first-order autoregressive process), as follows

$$\begin{aligned} \hat{B}_{x,i} &= \alpha \hat{B}_{x,i-1} + n_{x,i} \\ \hat{B}_{y,i} &= \alpha \hat{B}_{y,i-1} + n_{y,i} \\ \hat{B}_{z,i} &= \alpha \hat{B}_{z,i-1} + n_{z,i} \end{aligned} \tag{B.1}$$

where the dependence on the location and orientation parameters, (a,b,c,m,n,p), is omitted for brevity. The parameter α denotes the degree of correlation between sensor measurements, and is generally selected as $|\alpha| < 1$ in order to ensure weak-sense stationarity of the random process. $(n_{x,i}, n_{y,i}, n_{z,i})$ are assumed to be zero-mean Gaussian random variables with variance σ^2.

The inverse of the covariance matrix for this AR(1) process is a special case of the general scenario of an AR(p) process (i.e. an autoregressive process of order p) (see [37], equation (3)):

$$\mathbf{\Sigma}^{-1} = \frac{1}{\sigma^2}\left(\mathbf{I}_N + \alpha^2\mathbf{F} - \alpha\mathbf{G}\right) \tag{B.2}$$

where $\mathbf{I}_N$ is an $3N \times 3N$ identity matrix, $\mathbf{F}$ is an $3N \times 3N$ identity matrix with the first and last ones set to zero, and $\mathbf{G}$ is an $3N \times 3N$ matrix with ones along the first minor diagonals and zero elsewhere. Note that for the case of spatially uncorrelated sensor measurements (i.e. $\alpha = 0$), equation (B.2) reduces to $\mathbf{\Sigma}^{-1} = \frac{1}{\sigma^2}\mathbf{I}_N$ in line with the i.i.d. Gaussian scenario assumed earlier.

With the above definitions in place, it can be shown that the inverse of the covariance matrix has a tridiagonal, or Toeplitz structure. For the sake of clarity, we give a small example of this matrix for N=4:

$$\mathbf{\Sigma}^{-1} = \frac{1}{\sigma^2}\begin{bmatrix} 1 & -\alpha & 0 & 0 \\ -\alpha & 1+\alpha^2 & -\alpha & 0 \\ 0 & -\alpha & 1+\alpha^2 & -\alpha \\ 0 & 0 & -\alpha & 1 \end{bmatrix} \tag{B.3}$$

Substituting (B.2) into the right-hand side of equation (A.2), we can write

$$\begin{aligned} \log p\left(\hat{\mathbf{B}}\middle|\boldsymbol{\varepsilon}\right) &= \log\frac{1}{\left[2\pi\sigma^2\right]^{K/2}} - \frac{1}{2}\left(\hat{\mathbf{B}}-\mathbf{B}\right)^T \mathbf{\Sigma}^{-1}\left(\hat{\mathbf{B}}-\mathbf{B}\right) \\ &= \log\frac{1}{\left[2\pi\sigma^2\right]^{K/2}} - \frac{1}{2\sigma^2}\left(\hat{\mathbf{B}}-\mathbf{B}\right)^T\left(\mathbf{I}_N + \alpha^2\mathbf{F} - \alpha\mathbf{G}\right)\left(\hat{\mathbf{B}}-\mathbf{B}\right) \\ &= \log\frac{1}{\left[2\pi\sigma^2\right]^{K/2}} - \frac{1}{2\sigma^2}\left(\hat{\mathbf{B}}-\mathbf{B}\right)^T \mathbf{I}_N\left(\hat{\mathbf{B}}-\mathbf{B}\right) \\ &\quad - \frac{\alpha^2}{2\sigma^2}\left(\hat{\mathbf{B}}-\mathbf{B}\right)^T \mathbf{F}\left(\hat{\mathbf{B}}-\mathbf{B}\right) + \frac{\alpha}{2\sigma^2}\left(\hat{\mathbf{B}}-\mathbf{B}\right)^T \mathbf{G}\left(\hat{\mathbf{B}}-\mathbf{B}\right) \end{aligned} \tag{B.4}$$

For convenience and clarity, we introduce the following shorthand notation

$$\begin{aligned} \Delta B_{x,i} &= \hat{B}_{x,i} - B_{x,i} \\ \Delta B_{y,i} &= \hat{B}_{y,i} - B_{y,i} \\ \Delta B_{z,i} &= \hat{B}_{z,i} - B_{z,i} \end{aligned} \tag{B.5}$$

Assuming both $\hat{\mathbf{B}}$ and $\mathbf{B}$ to be $3N \times 1$ vectors (3 spatial magnetic field components for each sensor measurement), and exploiting the special structures of matrices $\mathbf{F}$ and $\mathbf{G}$, the right-hand side of (B.4) can be rewritten as

$$\begin{aligned} \log p\left(\hat{\mathbf{B}}\middle|\boldsymbol{\varepsilon}\right) &= \log\frac{1}{\left[2\pi\sigma^2\right]^{K/2}} - \frac{1}{2\sigma^2}\sum_{i=1}^{N}\left[\left(\Delta B_{x,i}\right)^2 + \left(\Delta B_{y,i}\right)^2 + \left(\Delta B_{z,i}\right)^2\right] \\ &\quad - \frac{\alpha^2}{2\sigma^2}\left[\left(\Delta B_{y,1}\right)^2 + \left(\Delta B_{z,1}\right)^2 + \sum_{i=2}^{N-1}\left[\left(\Delta B_{x,i}\right)^2 + \left(\Delta B_{y,i}\right)^2 + \left(\Delta B_{z,i}\right)^2\right] + \left(\Delta B_{x,N}\right)^2 + \left(\Delta B_{y,N}\right)^2\right] \\ &\quad + \frac{\alpha}{\sigma^2}\left[\sum_{i=1}^{N-1}\Delta B_{x,i}\Delta B_{x,i+1} + \sum_{i=1}^{N-1}\Delta B_{y,i}\Delta B_{y,i+1} + \sum_{i=1}^{N-1}\Delta B_{z,i}\Delta B_{z,i+1} + \Delta B_{y,1}\Delta B_{x,N} + \Delta B_{z,1}\Delta B_{y,N}\right] \end{aligned} \tag{B.6}$$

To compute the jk-element of the Fisher matrix, we take the partial derivatives of both sides of (B.6) with respect to ε_j and ε_k and substitute into equation (7). In order to facilitate this, the following relations can be obtained by using the chain rule for partial derivatives:

$$\frac{\partial}{\partial \varepsilon_j}\left(\Delta B_{x,i}\right)^2 = -2\Delta B_{x,i}\frac{\partial B_{x,i}}{\partial \varepsilon_j}$$
$$\frac{\partial}{\partial \varepsilon_j}\left(\Delta B_{y,i}\right)^2 = -2\Delta B_{y,i}\frac{\partial B_{y,i}}{\partial \varepsilon_j} \tag{B.7}$$
$$\frac{\partial}{\partial \varepsilon_j}\left(\Delta B_{z,i}\right)^2 = -2\Delta B_{z,i}\frac{\partial B_{z,i}}{\partial \varepsilon_j}$$

where the partial derivatives $\frac{\partial B_{x,i}}{\partial \varepsilon_j}$, $\frac{\partial B_{y,i}}{\partial \varepsilon_j}$ and $\frac{\partial B_{z,i}}{\partial \varepsilon_j}$ can be readily obtained by differentiating both sides of (3), (4) and (5) with respect to ε_j.

The third term on the right-hand side of (B.6) includes some product terms. The partial derivatives of these terms can be computed using the product rule:

$$\frac{\partial}{\partial \varepsilon_j}\left(\Delta B_{x,i}\Delta B_{x,i+1}\right) = -\Delta B_{x,i}\frac{\partial B_{x,i+1}}{\partial \varepsilon_j} - \Delta B_{x,i+1}\frac{\partial B_{x,i}}{\partial \varepsilon_j}$$
$$\frac{\partial}{\partial \varepsilon_j}\left(\Delta B_{y,i}\Delta B_{y,i+1}\right) = -\Delta B_{y,i}\frac{\partial B_{y,i+1}}{\partial \varepsilon_j} - \Delta B_{y,i+1}\frac{\partial B_{y,i}}{\partial \varepsilon_j}$$
$$\frac{\partial}{\partial \varepsilon_j}\left(\Delta B_{z,i}\Delta B_{z,i+1}\right) = -\Delta B_{z,i}\frac{\partial B_{z,i+1}}{\partial \varepsilon_j} - \Delta B_{z,i+1}\frac{\partial B_{z,i}}{\partial \varepsilon_j} \tag{B.8}$$
$$\frac{\partial}{\partial \varepsilon_j}\left(\Delta B_{y,1}\Delta B_{x,N}\right) = -\Delta B_{y,1}\frac{\partial B_{x,N}}{\partial \varepsilon_j} - \Delta B_{x,N}\frac{\partial B_{y,1}}{\partial \varepsilon_j}$$
$$\frac{\partial}{\partial \varepsilon_j}\left(\Delta B_{z,1}\Delta B_{y,N}\right) = -\Delta B_{z,1}\frac{\partial B_{y,N}}{\partial \varepsilon_j} - \Delta B_{y,N}\frac{\partial B_{z,1}}{\partial \varepsilon_j}$$

Taking the partial derivative of both sides of (B.6) and substituting the relations from (B.7) and (B.8), the partial derivative of $\log p\left(\hat{\mathbf{B}}\middle|\boldsymbol{\varepsilon}\right)$ with respect to ε_j can be obtained. The same relations in (B.7) and (B.8) can be used to obtain the partial derivative $\log p\left(\hat{\mathbf{B}}\middle|\boldsymbol{\varepsilon}\right)$ with respect to ε_k, by simply replacing ε_j with ε_k. With these two partial derivatives in hand, the *jk*-element of the Fisher matrix, $\mathbf{J}_{\boldsymbol{\varepsilon}}$, can be readily obtained using equation (7). The exact form of the different elements of the Fisher matrix is complex (largely due to the more complicated nature of the covariance matrix and its inverse as given in equation (B.2)) and is therefore omitted in the interests of brevity.